Journal of South American Earth Sciences 107 (2021) 102982

Contents lists available at ScienceDirect

Journal of South American Earth Sciences

journal homepage: www.elsevier.com/locate/jsames

Multi-proxy case study of a Neoproterozoic rhyolite flow in southernmost Brazil: Emplacement mechanisms and implications for ancient felsic lavas

Maurício Barcelos Haag [a,*], Rayane Bastos de Freitas [a], Carlos Augusto Sommer [a], Jairo Francisco Savian [a], Evandro Fernandes Lima [a], Johnathan Henrique Gambeta [a], Diego da Silveira Lyra [a], Ricardo Ivan Ferreira da Trindade [b]

[a] Instituto de Geociências, Universidade Federal do Rio Grande do Sul, Av. Bento Gonçalves, 9500, Porto Alegre, Rio Grande do Sul, Brazil
[b] Instituto de Astronomia, Geofísica e Ciências Atmosféricas, Universidade de São Paulo, Rua do Matão, 1226, São Paulo, São Paulo, Brazil

ARTICLE INFO

Keywords:
Rhyolite flow
Emplacement
Rheology
AMS
High-silica lava

ABSTRACT

Rhyolites compose an important record in the volcanic history of Earth, with significant occurrences in volcanic arcs, large igneous provinces and post-collisional terranes, often associated with explosive events. In several geologic provinces, rhyolites dominate as the most expressive geologic units (e.g., Silicic Large Igneous Provinces - SLIPs). Despite their importance, several aspects related to the emplacement of rhyolite flows are still enigmatic. Recent studies in modern rhyolite lavas suggest similar emplacement mechanisms to basaltic lavas, implying a more dynamic growth model for silicic flows, including outbreak lobes and outpour structures. Despite these advances, studies related to the recognition of these features in ancient flows are still rare. In this work we perform a multi-proxy study of an ancient (Neoproterozoic) rhyolitic lava flow combining fieldwork, petrography, geochemistry, rheology and magnetic fabric analysis. The Cerro do Perau outcrop (CP, southern Brazil) consists of a natural laboratory for the study of rhyolite lavas, presenting excellent exposure of a partially preserved flow with distinct flow features and folds. CP flow consists of a high-silica and low-crystal content rhyolite, suggesting its emplacement as an obsidian flow. Rheology data indicates high liquidus temperatures (>957 °C), with maximum viscosities of $10^{8.5}$ Pa s and glass transition temperatures (T_g) of 750 °C. The absence of brittle features suggests little to none displacement below T_g. Structural analysis indicates the predominance of sub-vertical foliation planes, including axial planes of folds, indicative of proximal (near-vent) regions in rhyolite flows. The absence of lineations favors a predominantly planar accommodation of the flow-induced deformation, which is confirmed by the shape of the magnetic fabric ellipsoids. Several of these ellipsoids display a high degree of anisotropy, mostly related to an oblate fabric, indicative of the development of high-strain zones within the flow. Our data suggest that CP flow presents some similarities with recently proposed field-based emplacement models for rhyolitic flows, highlighting the significant data that can be extracted from a combination of magnetic fabrics and rheological analyses.

1. Introduction

Rhyolites compose an expressive group of volcanic rocks, with extensive occurrence throughout the geological time. Despite this importance, several aspects related to the emplacement mechanisms of rhyolitic lavas are still enigmatic (Tuffen et al., 2013). While basalts occur in almost every tectonic setting (from mid-ocean ridges to volcanic belts), the presence of rhyolites requires either a high degree of magma differentiation or partial melting of the crust; hence their occurrence concentrates along with volcanic belts, post-collisional terranes, and a few large igneous provinces (e.g., Whitsunday; Bryan et al., 2002). As a result, our general understanding of the emplacement of basaltic lavas is remarkably greater, with both modern and ancient case studies available (e.g. Walker, 1967; Pinkerton and Sparks, 1978; Single and Jerram, 2004; Guest et al., 2012; Vye-Brown et al., 2013; Bernardi et al., 2015) when compared to rhyolitic lavas. Rhyolites also predominate as end-members of bimodal, anorogenic magmatic systems (Bryan et al., 2002), which denotes their geodynamic relevance to magmatism on Earth throughout time. Because of its higher silica content, silicic magmas generally erupt explosively, producing abundant pyroclastic

* Corresponding author.
E-mail address: mauricio.haag@ufrgs.br (M.B. Haag).

https://doi.org/10.1016/j.jsames.2020.102982
Received 16 April 2020; Received in revised form 7 October 2020; Accepted 20 October 2020
Available online 12 November 2020

density currents and ignimbrite deposits (Di Genova et al., 2017), with a few historic records of rhyolitic lava flows (Cas and Wright, 1987). As a consequence, a greater number of works have focused on the study of explosive deposits (e.g. Elston and Smith, 1970; Wilson et al., 2005; Finn et al., 2015; Alva-Valdivia et al., 2017; Nakagawa et al., 2018), while the structural emplacement of rhyolitic lava flows is still poorly constrained, with just a few modern and ancient case studies (e.g. Fink, 1980; Manley and Fink, 1987; Tuffen et al., 2013; Bullock et al., 2018; Leggett et al., 2020).

Despite their discrete occurrence, the study of these flows may be a key factor for understanding the emplacement mechanisms of silicate melts, which is ultimately controlled by melt rheology (Cassidy et al.,

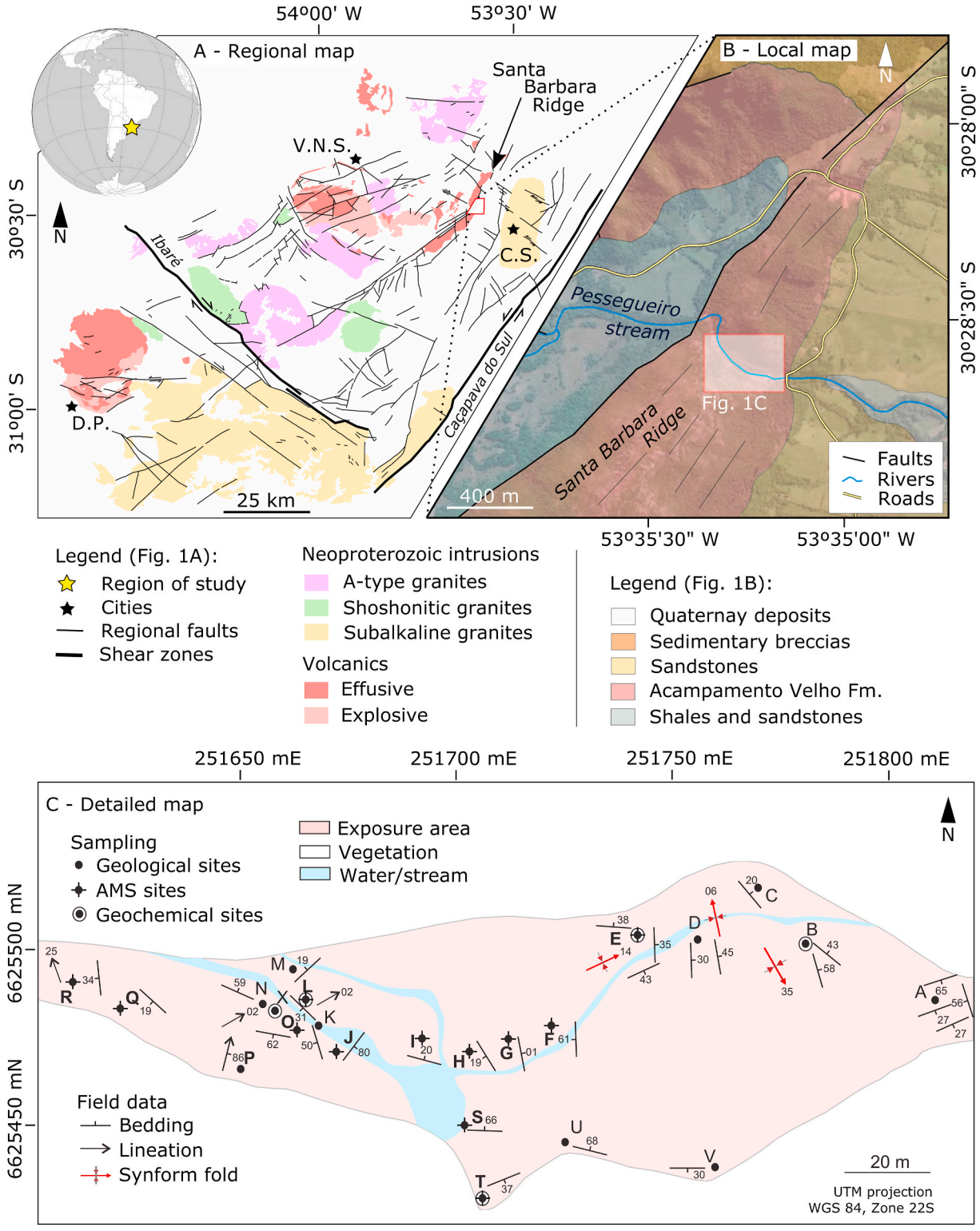

Fig. 1. Location map of the studied area: (A) distribution of the Neoproterozoic silicic magmatism in southern Brazil, adapted from Hartmann et al. (2007); cities: Caçapava do Sul (C.S.), Dom Pedrito (D.P.) and Vila Nova do Sul (V.N.S.); (B) regional geological map of the studied area; (C) map of Cerro do Perau flow, showing the exposure area, geological, geochemical and AMS sampling sites.

2018). A few works highlighted the structural complexity of rhyolite flows, which includes the presence of variable wavelength folds, creases, flow banding, devitrification, and brecciation, among others features and processes (Manley and Fink, 1987; Fink, 1980; Leggett et al., 2020). The general knowledge about these rocks indicates that these flows occur as relatively large thickness, limited length flows, as a result of their high viscosity. Recent studies have challenged this length-limited model for silicic flows, with both modern (e.g. Tuffen et al., 2013) and more ancient case studies (e.g. Besser et al., 2018) revealing a more complex and dynamic nature for rhyolitic lava flows. In these case studies, flows can evolve through several breakout lobes, similar to basaltic lavas, forming complex flow units and resulting in extensive rhyolitic lava fields with high mobility (Manley, 1992; Tuffen et al., 2013). These findings show that the emplacement mechanisms of silicic flows still an open debate, with several questions regarding the rheological controls, the structural features, and process timescale on flow advance (Magnall et al., 2017; Leggett et al., 2020).

In this work, we apply a multi-proxy approach to the study of the Cerro do Perau outcrop (CP), an ancient (Neoproterozoic), partially preserved rhyolite flow present in southern Brazil. The CP composes a natural laboratory for the study of rhyolite flows, displaying complex structures, with abundant flow-induced folds and flow foliations (Zerfass et al., 2000) of primary origin. In order to constrain the emplacement mechanisms of this ancient flow, we conducted fieldwork, collected structural data and samples for anisotropy of magnetic susceptibility (AMS), petrography, and geochemistry analyses. Using this dataset, we derived basic rheological parameters (*liquidus* and glass transition temperatures, viscosity) and the structural patterns (using both AMS and field data) of CP. Finally, we used these results to build an emplacement model and constrain the emplacement of CP flow, comparing it with recent models and the implications of CP observations to rhyolitic lava flows. Our results indicate similar emplacement mechanisms to those observed in modern flows (e.g. Tuffen et al., 2013), suggesting a more dynamic emplacement style for rhyolitic flows.

2. Geological setting

The CP, located in southern Brazil (Fig. 1A), is part of the Acampamento Velho Fm., a Neoproterozoic undeformed volcanic succession characterized by intense magmatism between 574 ± 7 Ma and 549 ± 5 Ma (Sommer et al., 2005; Janikian et al., 2008; Matté et al., 2016), marked by the presence of abundant pyroclastic and effusive silicic deposits (Sommer et al., 1993; Zerfass et al., 2000; Wildner et al., 2002). The CP composes a partially preserved rhyolitic lava flow which stands out for its excellent exposure and preservation of flow-induced bands and folds (Zerfass et al., 2000). The outcrop presents an approximate area of 10,000 m^2, and is located next to the Pessegueiro stream in the Santa Barbara ridge, a NE-SW prominent structure in the region (Fig. 1B).

The Acampamento Velho Fm. comprises the most extensive silicic subaerial volcanic succession in southern Brazil, developed in the post-collisional setting of the Brasiliano-Pan-African orogeny (Lima et al., 2007). This period was marked by intense plutonism, volcanism, and sedimentation along localized strike-slip basins currently grouped in the Camaquã Basin (Sommer et al., 2013). One important characteristic of this period is the occurrence of several granitoid intrusions (Fig. 1A) along with the intense silicic volcanism of Acampamento Velho Fm., as revealed by field data and available radiometric ages (Lima et al., 2007; Matté et al., 2016). In this context, the Acampamento Velho Fm. represents the extrusive manifestation of a sodic, silicic saturated magmatism, where the volcanic products are mostly ignimbrites, rheoignimbrites and rhyolitic flows (Wildner et al., 2002; Sommer et al., 2005; Lima et al., 2007). The volcanic deposits show a remarkable volume, forming ignimbrite plateaus with areas of up to 400 km^2 and thicknesses of 100 m (Lima et al., 2007; Sommer et al., 2013). The stratigraphic analysis of the deposits shows that eruptive cycles usually began with explosive eruption followed by lava flows, suggesting a decrease in the volatile activity throughout the eruptive cycle (Sommer et al., 2013).

3. Methodology

3.1. Fieldwork

The fieldwork involved detailed geological mapping and structural measurements were performed using a magnetic compass and GPS receptor. The field data was processed and compiled using ArcMap 10.5 (ESRI), while the structural data was analyzed using contour plots processed in Stereonet 10 (Cardozo and Allmendinger, 2013). The fieldwork also included sampling for geochemical, petrographic and magnetic fabric analyses.

3.2. Geochemistry and petrography

Six representative samples were selected for whole-rock geochemical analysis. The chemical analysis was carried out at Acme Analytical Ltd (Vancouver, Canada) using the methods of ICP-AES (Inductively Coupled Plasma Atomic Emission Spectroscopy) for major elements and ICP-MS (Inductively Coupled Plasma Mass Spectrometry) for minor and trace elements. Seven thin sections were prepared using representative samples of CP. The samples were analyzed using a Leica DM4500 digital microscope model with an attached camera (LEICA DFC495 model).

3.3. Rheology

Based on geochemical data, we estimated rheological parameters for Cerro do Perau melts using the numerical models of Sisson and Grove (1993) and Giordano et al. (2008). Using the model of Sisson and Grove (1993), we estimated the liquidus temperature (T_L), while the model of Giordano et al. (2008) was applied to the determination of both melt viscosity (η) and the glass transition temperature (T_g). The T_g parameter reflects the boundary temperature between a ductile (above T_g, allowing viscous flow, pyroclastic sintering and welding) and a fragile (below T_g, allowing only elastic deformation) behavior of a silicate melt (Giordano et al., 2005). In order to evaluate the effect of dissolved water over the melt rheology, viscosity was estimated using both anhydrous and wet compositions containing 0.25 and 0.5 wt% of H_2O.

3.4. Anisotropy of magnetic susceptibility (AMS)

The Anisotropy of low-field magnetic susceptibility (AMS) allows the determination of the petrofabrics of rocks, through the measurement of the orientation of the minerals present in the samples (e.g., Graham, 1954; Tarling and Hrouda, 1993). The AMS technique has been extensively applied in flow direction studies, considering the limitations in defining magmatic fabrics and flow structures using only compass field measurements. The technique consists of measuring the magnetic susceptibility (κ) of a sample in different directions, defining the magnitude (intensity and orientation) of the three principal axes $K_1 \geq K_2 \geq K_3$ of magnetic susceptibility (Tarling and Hrouda, 1993). These axes ultimately represent the overall orientation of the particles present in the sample, allowing the definition of the rock petrofabrics. Using the obtained AMS tensor we are able to define both the magnetic foliation (which pole is marked by K_3, the minor anisotropy axis) and the magnetic lineation (marked by K_1, the major anisotropy axis) of a given sample. This definition allows the determination of flow directions, as well as strain patterns and intensities (e.g., Cañón-Tapia, 2005).

For AMS analyses, 12 representative sites were sampled using a portable gasoline-powered non-magnetic drill. Each site consisted of at least 10 oriented cores. At the laboratory, the cores were cut into specimens with 2.5 cm in diameter and 2.2 cm in height, using a diamond-coated wheel saw, totalizing 254 standard specimens. The

AMS measurements were performed at the Laboratory of Paleomagnetism and Geomagnetism of University of Sao Paulo (USPMag), using a MFK1-A apparatus (Agico Ltd.) operating in a low alternating field (200 A/m) at 976 Hz. Directional data were processed using Anisoft5 (Agico Ltd.), which allowed the visualization of both AMS axes and the scalar results. Bootstrap statistics was applied to our results in order to assist the main magnetic tensor evaluation and the determination of flow patterns (Tauxe et al., 1991).

3.5. Magnetic mineralogy

The magnetic mineralogy and domain states of ferromagnetic phases on the magnetic fabric is fundamental in studies for the determination of flow directions in pyroclastic deposits and lava flows (e.g., Rochette et al., 1999; Moncinhatto et al., 2020). In order to evaluate our interpretation of magnetic fabric, we performed a magnetic mineralogy characterization at USPMag using thermomagnetic curves, isothermal remanent magnetization (IRM), hysteresis loops and first-order reversal curves (FORC) diagrams. Thermomagnetic curves (e.g., Petrovsky and Kapicka, 2006) were obtained measuring low-field magnetic susceptibility on 3 representative powdered samples through heating and cooling cycles from −195 °C up to 700 °C under Ar atmosphere, using a CS-L cryostat and CS-4 furnace coupled to a Kappabridge KLY-4S susceptibility meter (Agico Ltd.). The resulting thermomagnetic curves were analyzed in the Cureval 8 program (www.agico.com; Hrouda et al., 1997). The Curie temperatures (T_C) were determined by a method based on inflection point on the decreasing branch of susceptibility curve, which marks the beginning of the paramagnetic hyperbola just at the T_C (Petrovský and Kapička, 2006). For both hysteresis and IRM acquisition curves, small rock chips of 9 representative samples were measured by applying fields of up to 1 T using a Princeton Measurement Corporation MicroMag 3900 vibrating sample magnetometer (VSM). FORC diagrams (Roberts et al., 2000) were obtained for 4 representative samples at room temperature after 200 reversal curves with an average time of 200 ms, and data were processed using the FORCinel software package (Harrison and Feinberg, 2008), with a smoothing factor of 5.

3.6. Scanning electron microscopy

To evaluate the spatial distribution of magnetic minerals, two representative thin sections were studied using a Scanning Electron Microscope (SEM) model Jeol JSM 6610-LV operated at a beam voltage of 15 kV, at the Laboratory of Isotopic Geology (LGI-UFRGS). Mineral distribution was determined using backscattered electron (BSE) images, while Ti and Fe presence was determined using energy dispersive spectroscopy (EDS).

4. Results

4.1. Field and petrographic aspects

CP rocks are characterized by rhyolites with remarkable flow foliations (Fig. 2). Magmatic folds and foliations are widespread, pervasive over the entire site and show an almost chaotic distribution over the outcrop. The observed structures include both metric (Fig. 2A) and centimetric folds (Fig. 2B), of variable orientations and wavelengths. Another characteristic pattern observed at CP is the presence of millimetric flow layers (Fig. 2C), which are marked by alternating levels of devitrification. These layers are continuous across several meters, being coherent with the more spaced, tabular foliations. In contrast, lineations are virtually absent in the entire outcrop. Some regions present distinct structures (Fig. 2D) composed of a high dipping plane, which gradually becomes horizontal, resembling outpour structures in feeding systems.

Petrographically, the rhyolites of CP are aphanitic hemicrystalline, localized porphyritic. The percentage of phenocrysts is very low (less than 5%) and is represented by quartz and K-feldspar, which occur in association with microfenocrystals of opaque minerals (0.2 mm) and zircon. In all cases, the content of crystals is lower than 5%, and their presence localized along the foliation planes. The matrix is represented by a thin mosaic of quartz-feldspar microliths and crystallites. Several

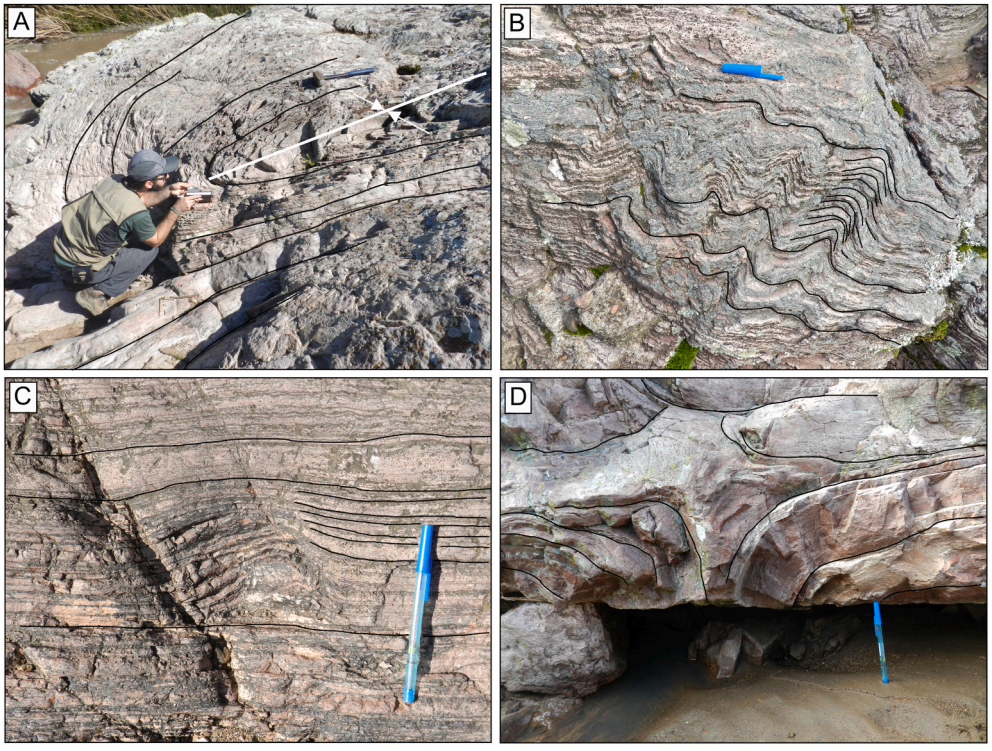

Fig. 2. Field aspects observed at CP: (A) metric size synform, isoclinal fold, (B) decimetric convolute folds, (C) millimetric flow lamination marked by different devitrification phases and (D) outpour structure resembling a feeding zone of a possible breakout lobe. The pen is 15 cm long.

devitrification textures are observed, including spherulites with necklace-like morphologies (Fig. 3A) and a mean diameter of 200 mm. Flow foliation is sometimes enhanced by levels with a higher degree of crystallinity and may have an incipient pattern, which sometimes involves phenocrysts. The presence of fine levels with distinct granularities consisting of quartz, feldspar and opaque minerals is also a common feature (Fig. 3B). The foliation is frequently marked by pre-existing crystals, such as millimetric zircon crystals (Fig. 3C), suggesting effective mechanical orientation of these particles during flow emplacement. Resorption features are common in quartz phenocrysts, highlighting the corrosion gulfs and the amoeboid geometry of some crystals (Fig. 3D).

4.2. Geochemistry

Chemical whole-rock analyses of six representative samples were performed to investigate the composition and rheology of Cerro do Perau melts (spatial distribution of samples presented in Fig. 1C). CP rocks generally have SiO_2 values higher than 74 wt% (Table 1; please check supplementary item 1 for a complete geochemical table) and can be considered as high silica type rhyolites (Mahood and Hildreth, 1983).

The CP rocks are related to subalkaline series where samples show trends situated close to the boundary between silica-saturated alkaline fields, as displayed on R_1-R_2 (Fig. 4A; De la Roche et al., 1980) and the SiO_2 versus Zr/TiO_2 diagram (Supplementary item 2; Winchester and Floyd, 1977). All samples display high contents of alkalis ($Na_2O + K_2O$ > 8.4 wt%) and low contents of Al_2O_3, CaO and MgO, with agpaitic indices higher than 0.8, typical values for alkaline rhyolites (Ewart, 1979).

Trace element patterns of CP rhyolites normalized against ocean-ridge granite (ORG) values (Pearce et al., 1984) are displayed in Fig. 4B, where all Acampamento Velho Fm. rhyolites show a similar pattern with low Ba and Sr values associated with high HFSE (high-field strength elements) contents, which is typical of rocks with alkaline affinity. In the granitoid classification diagrams proposed by Whalen et al. (1987), all samples plot in the "A" type granite field (Supplementary item 2), which are alkaline and anorogenic. This classification is also confirmed by the values of (10000 * Ga)/Al > 2.6, Ce + Y + Nb + Zr > 500 ppm and FeOt/FeOt + MgO > 0.9.

4.3. Rheology

Using the method proposed by Sisson and Grove (1993), we obtained almost uniform *liquidus* temperatures (T_L) for Cerro do Perau melts, considering its homogeneous composition, with T_L values ranging from 957 to 963 °C. The calculated melt viscosity using the model of Giordano et al. (2008) at T_L ranged from $10^{8.0}$ to $10^{8.5}$ Pa s. The simulated addition of water to our samples led to a considerable decrease in melt viscosity, obtaining a melt 10 times less viscous with the addition of only 0.25 wt % of H_2O (Fig. 5). The glass transition temperature (T_g) calculated using the model of Giordano et al. (2008) resulted in values ranging from 745 to 759 °C.

4.4. Magnetic mineralogy

Using a combination of thermomagnetic curves, IRM acquisition curves, hysteresis loops we were able to characterize the magnetic mineralogy present in the study area, defining three distinct patterns resulting from a combination of ferromagnetic assemblages with distinct coercivities (Fig. 6).

Behavior 1 is marked by high-temperature curves displaying at least major drops in susceptibility at ~598 and ~680 °C (Fig. 6A), suggesting the presence of at least two magnetic phases. These temperatures are compatible with both Curie and Néel temperatures for magnetite and hematite, where the presence of magnetite can be inferred by a poorly define transition around −150 °C (Hunt et al., 1995). IRM curves indicate that the samples did not reach the saturation, and suggest a mixture of low (at least 60%) and high coercivity magnetic phases (Fig. 6B). Hysteresis loops show a narrow wasp-waisted plot, also suggesting a mix

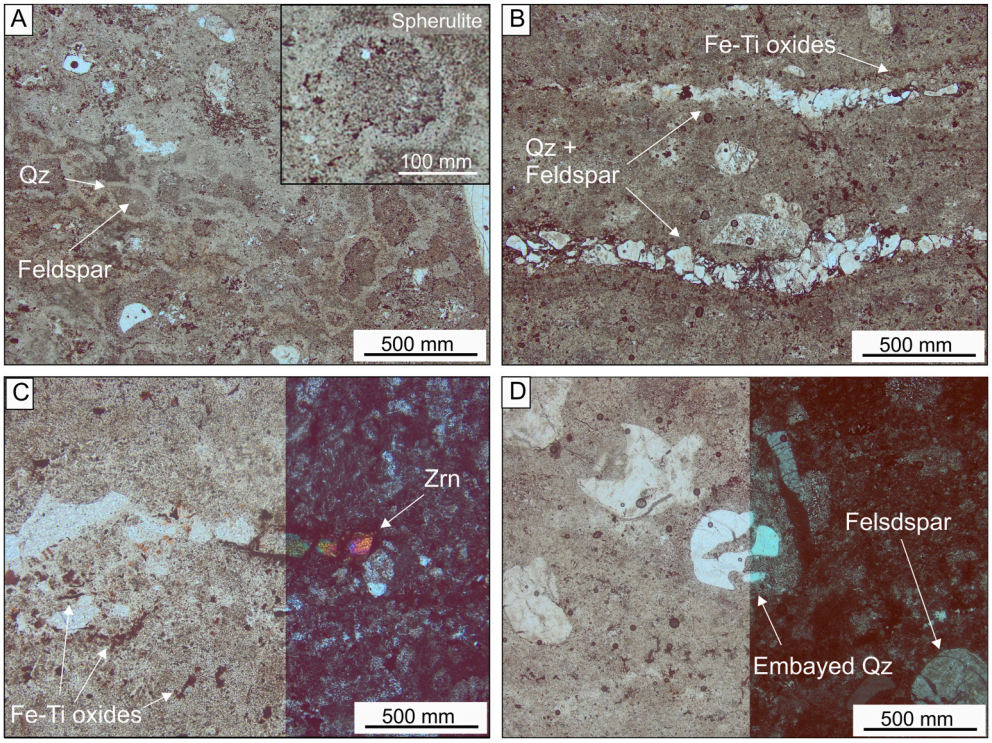

Fig. 3. Representative microscopic features Cerro do Perau samples: (A) abundant spherulites, (B) late devitrification phases defined by quartz and feldspar, (C) zircon forming flow foliation, (D) embayed quartz phenocryst. All pictures obtained under polarized light, with exception to the right section of (C) and (D), which were obtained under crossed polarizers. Abbreviations: quartz (Qz) and zircon (Zrn).

Table 1
Whole-rock analysis from Cerro do Perau, major and minor elements (% by weight). Coordinates respective to UTM zone 22S, datum WGS 1984.

Sampling sites	B	E	T	L1	X	L2
UTM (mE)	251781	251742	251706	251665	251660	251665
UTM (mN)	6625501	6625503	6625442	6625488	6625483	6625488
SiO_2	75.38	75.40	76.08	74.43	74.91	75.58
TiO	0.13	0.14	0.13	0.14	0.14	0.13
Al_2O_3	12.40	12.58	12.02	13.09	13.01	12.44
Fe_2O_3	1.70	1.74	2.23	2.02	1.77	1.76
MnO	0.02	0.02	0.01	0.03	0.02	0.02
MgO	0.12	0.14	0.12	0.17	0.17	0.15
CaO	0.34	0.17	0.17	0.16	0.13	0.19
Na_2O	2.55	2.80	2.12	2.64	2.94	2.62
K_2O	5.78	5.60	5.53	5.75	5.49	5.65
P_2O_5	<0.01	0.01	<0.01	0.02	0.01	<0.01
LOI	1.4	1.2	1.4	1.4	1.2	1.3
Total	99.86	99.86	99.88	99.88	99.89	99.87

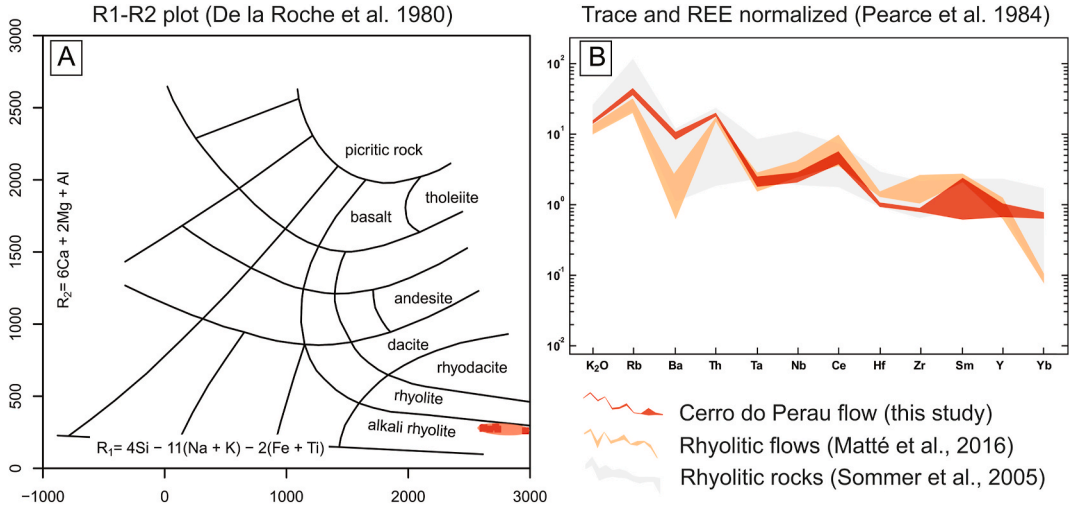

Fig. 4. (A) R1-R2 classification diagram (De la Roche et al., 1980) showing the distribution of Cerro do Perau samples and (B) trace and REE diagram normalized to org (Pearce et al., 1984) showing a comparison of Cerro do Perau samples and other silicic rocks of the Acampamento Velho Fm.

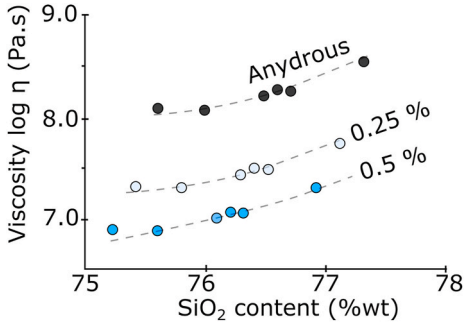

Fig. 5. Rheological results for Cerro do Perau melts and the estimated effect of the variable amounts of water (0, 0.25 and 0.5 %wt) on the melt viscosity.

of minerals with contrasting coercivities (Fig. 6C; Roberts et al., 1995; Tauxe et al., 1996). This behavior was observed in site L.

Behavior 2 is characterized by a gradual, noisy decrease in magnetic susceptibility (Fig. 6D). However, the heating curve shows the first drop at ~582 °C, suggesting the presence of magnetite. In addition, the heating curve continue dropping until 681 °C, suggesting the presence of hematite. In the low-temperature curves, two transitions are present, one around −153 °C and the other, poorly defined, starting at −50 °C (Fig. 6D). High and low transition temperatures are compatible with Ti-magnetite and hematite (Hunt et al., 1995; Lattard et al., 2006). IRM curves show that the sample did not reach the saturation (Fig. 6E), indicating high coercivity phases in major proportion when compared to behavior 1. Hysteresis loops (Fig. 6F) show a distinct wasp-waisted pattern, suggesting a mixture of minerals with hard and soft coercivities (Roberts et al., 1995; Tauxe et al., 1996). This behavior predominates in the studied samples, being observed in sites E, G, J, O, R and S.

Behavior 3 presents a rather noisy thermomagnetic signal, with a gradual decrease in magnetic susceptibility above 515 °C (Fig. 6G). The rate of decrease increases above 600 °C on approach to the Néel temperature of hematite. Low-temperature curves display two transitions, one at ca. −174 °C (possibly magnetite) and other at ca. −19 °C (possibly hematite). IRM curves indicate a predominance of high-coercivity minerals, which remain unsaturated with fields of up to 1T (Fig. 6H). Hysteresis loops indicate a mix of minerals with contrasting coercivities (Fig. 6I), as observed in behaviors 1 and 2. This behavior was observed in site T.

Although largely used in paleomagnetic and AMS studies, IRM acquisition curves and hysteresis loops provide only a measure of the bulk magnetic properties in the studied samples (e.g., Roberts et al., 2017, 2018, 2019). In the case of mixed magnetic assemblages, the magnetic characterization usually requires the acquisition of FORC diagrams (Roberts et al., 2000), which can provide information about the grain size and domain state of magnetic minerals. FORC analysis is shown for representative samples (Fig. 7). Overall, the FORC distribution is centered in Bu = 0, with small differences in spread along the Bc

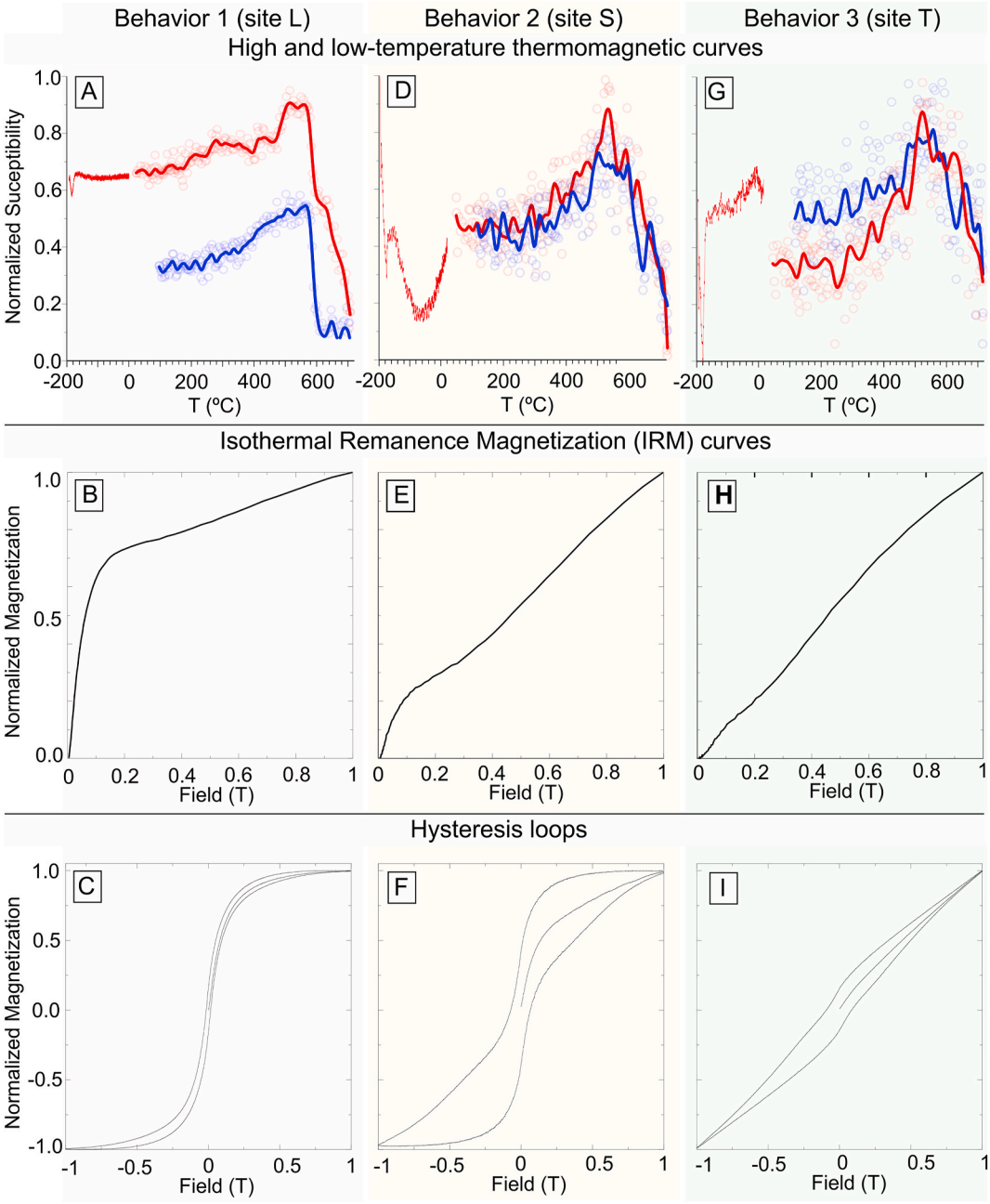

Fig. 6. Magnetic characterization of the studied samples showing the respective thermomagnetic, IRM curves and hysteresis loops for the identified three distinct behaviors: Behavior 1 (A–C), 2 (D–F), and 3 (G–I). Thermomagnetic and IRM curves are normalized.

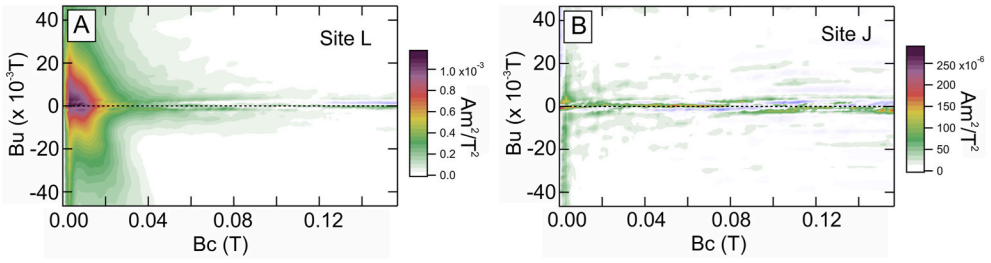

Fig. 7. Representative FORC diagrams of selected samples from CP flow: (A) predominance of MD Ti-magnetite grains and (B) weakly magnetic FORC distribution with MD particles.

(Fig. 7A). This component presents peak a coercivity of around 10–15 mT, with increased vertical spread and variability in the exact FORC structure that may actually represent more than one component. This FORC structure is often interpreted as MD particles (Roberts et al., 2017). In several samples, the weakly magnetic component is not evident, with low values FORC distribution (<250 × 10^{-3} Am^2/T^2, Fig. 7B). However, the vertical spread along the Bc is still observed, which is typical of MD grains. Please check supplementary items 3, 4 and 5 for additional IRM, hysteresis loops and FORC diagrams.

4.5. SEM observations

SEM analyses performed in two representative samples indicate the presence of a small amount of Fe–Ti oxides (Fig. 8A and B), mostly coarse grained, equant, crystals (around 200 μm) of Ti-magnetite (Fig. 8A) and hematite (Fig. 8B). EDS spectra indicate the presence of both Ti-magnetite (Fig. 8A) and hematite (Fig. 8B) as the main Fe–Ti oxides present in the samples. Based on EDS spectra, the molar Ti content (x) in the Ti-magnetite ($Fe_{3-x}Ti_xO_4$) ranges from 0.56 to 9.88%.

4.6. Structural and magnetic fabrics

A total of 12 sites were sampled in the CP, generating 254 specimens, with the mean AMS results (for each site) available in Table 2.

In general, CP samples present a low mean magnetic susceptibility (Km), with most values clustering around 40× 10^{-6} SI (Fig. 9A). The scalar results also show a positively skewed Gaussian distribution of magnetic susceptibilities, with Km ranging from 10 to 170 × 10^{-6} SI (Fig. 9A). Samples present a wide range of degree of anisotropy (P′, light-toned diamonds in Fig. 9B), from 1.003 to 3.18 (3%–218%, mean of 25%). When comparing average site values, sites with high P′ tend to show high Km values, as highlighted by sites I, L and S (solid squares in Fig. 9B). The shape parameter (T) of magnetic tensors indicates a predominance of oblate ellipsoids (T > 0, 74% of total), although several samples fall under the prolate (T < 0) and triaxial (T ca. 0) fields (Fig. 9C). With exception to site O, all other sites display a predominance of oblate tensors (Fig. 9C).

The AMS directional data was plotted in a sketch of the Cerro do Perau exposure, along with representative geologic structures (Fig. 10), in order to assist the structural analysis. Magnetic axes within each site are usually well-grouped (with exception to sites J, O, Q and R), allowing AMS based interpretations. In several sites (*e.g.*, H, F, and T) both K_1 (magnetic lineation) and K_2 girdle, suggesting the presence of strongly oblate ellipsoids, with a well-defined K_3 (pole of the magnetic foliation).

5. Discussion

5.1. Field and petrographic aspects

CP flows are characterized by extensive foliations and folds, while lineations are absent among the observed structures, suggesting little to none constrictional strain during the flow emplacement (Yang et al., 2019). The continuous character of the foliations observed in the CP suggests a prolonged viscous flow of the melt, a diagnostic feature of lava flows (Manley, 1992). The presence of folds in rhyolitic lavas results from the lateral movement and compression, leading to significant shear and development of folds (Smith and Houston, 1994). A critical aspect for fold development is the presence of contrasting rheological layers (Fink, 1980), which suggests that CP folds may have developed preferentially in the margins of the flow unit, where higher strain and rheological contrasts are expected to occur. In addition to that, the overall presence of upright folds in CP suggests that the current level of erosion probably marks the top region the flow (Christiansen and Lipman, 1966; Fink, 1980; Dragoni et al., 1992). The observed outpour structures may be associated with breakout lobes, as characterized by Tuffen et al. (2013), although no flow crust was identified in the field mapping. Petrographically, the low presence of crystals suggests little to none effect of these particles on the overall flow rheology (Lejeune and Richet, 1995; Castruccio et al., 2010). Some studies have shown that the origin of the textural heterogeneities in silicic volcanic units can be attributed to local chemical differences, particularly the volatile content (e.g., Fink and Manley, 1987), leading to the development of layers with distinct vesicularity patterns, degree of crystallinity, and color, as observed in most CP samples.

5.2. Geochemistry

The geochemical data of the CP rhyolites indicate a genetic link with the Acampamento Velho Fm. magmatism, with similar geochemical signatures to alkaline rhyolites of the Ramada Plateau (Sommer et al., 2005) and Taquarembó Plateau (Sommer et al., 1999) regions and related to the post-collisional Neoproterozoic type "A" magmatism in southern Brazil.

5.3. Rheology

All samples from Cerro do Perau present high silica content, suggesting a strong non-arrhenian behavior for these melts (Giordano et al., 2006). The obtained results of T_L are comparable to the temperatures for ignimbrites of the Acampamento Velho Fm., which ranged from 870 to 978 °C (Sommer et al., 2013). These values also match the generation temperature of A-type magmas (Patiño Douce, 1997), highlighted by the

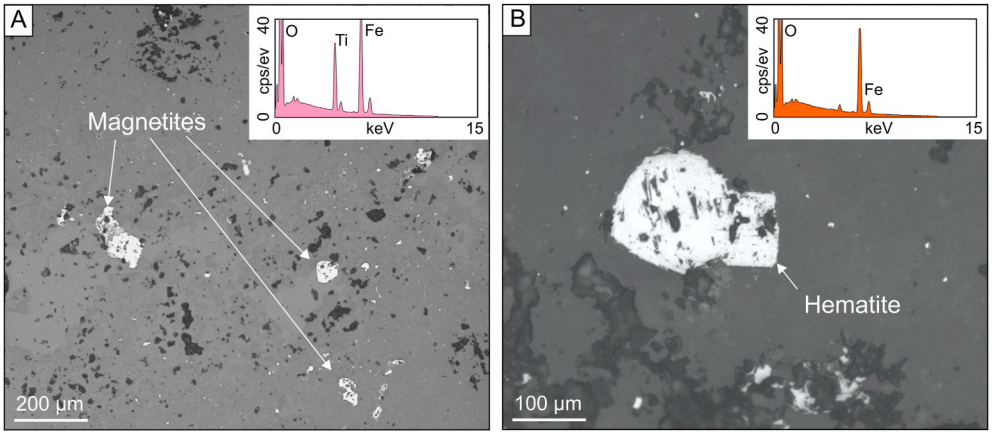

Fig. 8. SEM observations of CP flow: (A) group of magnetites and (B) hematite crystal. Representative EDS spectra of the Fe–Ti oxides in each image.

Table 2
AMS data from the studied sites. *n* = number of measured specimens; Km = mean magnetic susceptibility (SI units); L = magnetic lineation; F = magnetic foliation; P′ = degree of anisotropy; T = shape parameter (Jelinek, 1981); D = declination and I = inclination of the AMS principal axes K_1, K_2 and K_3; e and z: semi angles of the minor and major axes of the 95% confidence ellipse, respectively; Values in parentheses indicate the standard deviations *(σ)*. Coordinates respective to UTM zone 22S, datum WGS 1984.

Site	UTM coordinates		*n*	Scalar results					Directional results		
	mE	mN		Km (x 10^{-6}) *(σ)*	L *(σ)*	F *(σ)*	P′ *(σ)*	T *(σ)*	K_1 D, I *[e, z]*	K_2 D, I *[e, z]*	K_3 D, I *[e, z]*
E	251742	6625503	13	32.2 *(10.1)*	1.06 *(0.04)*	1.10 *(0.12)*	1.17 *(0.14)*	0.03 *(0.57)*	327, 62 *[020, 10]*	190, 20 *[045, 19]*	093, 16 *[045, 09]*
F	251722	6625482	17	43.0 *(8.1)*	1.03 *(0.04)*	0.89 *(1.2)*	1.23 *(0.17)*	0.67 *(0.28)*	147, 74 *[015, 02]*	036, 05 *[020, 11]*	305, 14 *[018, 03]*
G	251712	6625479	25	37.4 *(10.9)*	1.03 *(0.03)*	1.28 *(0.25)*	1.35 *(0.31)*	0.66 *(0.33)*	264, 48 *[018, 12]*	078, 41 *[059, 16]*	170, 03 *[059, 14]*
H	251703	6625476	29	40.6 *(17.3)*	1.04 *(0.04)*	1.28 *(0.22)*	1.37 *(0.28)*	0.61 *(0.37)*	276, 63 *[061, 07]*	146, 18 *[061, 21]*	049, 19 *[021, 07]*
I	251692	6625479	21	66.0 *(55.2)*	1.04 *(0.08)*	1.29 *(0.43)*	1.40 *(0.57)*	0.35 *(0.56)*	205, 64 *[018, 05]*	050, 23 *[046, 18]*	316, 09 *[046, 04]*
J	251672	6625476	17	27.2 *(8.1)*	1.01 *(0.01)*	1.01 *(0.01)*	1.02 *(0.01)*	0.08 *(0.44)*	246, 15 *[044, 34]*	076, 74 *[020, 10]*	337, 02 *[079, 40]*
L	251665	6625488	26	66.3 *(58.8)*	1.11 *(0.06)*	1.21 *(0.12)*	1.36 *(0.18)*	0.24 *(0.30)*	236, 80 *[048, 13]*	141, 08 *[084, 45]*	051, 09 *[084, 23]*
O	251663	6625481	19	25.9 *(12.6)*	1.06 *(0.04)*	1.15 *(0.34)*	1.25 *(0.42)*	−0.12 *(0.53)*	191, 22 *[073, 044]*	078, 41 *[073, 36]*	300, 39 *[049, 23]*
Q	251622	6625486	23	47.1 *(7.5)*	1.01 *(0.01)*	1.03 *(0.06)*	1.05 *(0.07)*	0.31 *(0.45)*	317, 49 *[076, 31]*	083, 26 *[076, 45]*	188, 28 *[049, 14]*
R	251611	6625453	24	31.7 *(5.8)*	1.02 *(0.02)*	1.02 *(0.04)*	1.04 *(0.06)*	0.01 *(0.40)*	210, 05 *[041, 28]*	305, 42 *[040, 38]*	115, 47 *[038, 32]*
S	251702	6625459	22	68.0 *(36.3)*	1.04 *(0.05)*	1.39 *(0.36)*	1.52 *(0.47)*	0.68 *(0.25)*	257, 65 *[016, 13]*	355, 03 *[032, 16]*	087, 23 *[032, 03]*
T	251706	6625442	25	30.5 *(9.9)*	1.02 *(0.03)*	1.10 *(0.20)*	1.13 *(0.28)*	0.20 *(0.54)*	227, 56 *[081, 11]*	018, 29 *[081, 09]*	116, 13 *[025, 08]*

spatio-temporal association of A-type granitoids with the Acampamento Velho Fm. in southern Brazil (Fig. 2A). The viscosity values are also similar to the results obtained by Sommer et al. (2013) for ignimbrites in the Acampamento Velho Fm., as well as other estimates for rhyolitic flows around the world (Fink, 1980; Závada et al., 2009; Bullock et al., 2018; Leggett et al., 2020). One important feature of CP flow is that it presents a very low crystal content, suggesting its emplacement as an obsidian flow and little to none effect of crystals over the melt viscosity (Lejeune and Richet, 1995). Petrographic features of CP indicate similarities with the shear banded lava observed in the obsidian Rocche Rosse flow, which is marked by low vesicularity and a high degree of anisotropy, resulting in the development of a strong strain fabrics (Shields et al., 2016).

Considering the effusive character of CP flow, the calculated Tg provides an estimation for the lower limit of the eruption temperature. The overall absence of brittle structures in the outcrop suggests a predominance of viscous (or ductile) behavior of the melt, with little to none flow movement after crossing T_g (745–759 °C), which would ultimately result in the development of brittle structures. This could be resulted by the development of a crust sufficiently strong to inhibit flow advance (Magnall et al., 2017; Leggett et al., 2020). It is important to note that slower cooling rates result in lower T_g values (Giordano et al., 2005), granting a wider 'ductile window' for the melt to deform or flow. This setting is expected to occur in slow cooling rates sections of a given flow unit, such as the flow core (Manley and Fink, 1987).

The simulated addition of walter resulted a considerably decrease in melt viscosity (Fig. 5). This 'hydrous Cerro do Perau melt' scenario would ultimately lead to lower viscosities and higher ascent rates in the conduit (Cassidy et al., 2018). This dynamic commonly results in less time for degassing, leading to explosive eruptions (Gonnermann and Manga, 2007), which is probably not the case for CP, which lacks fragmentation features and suggests a more effusive dynamics.

5.4. Magnetic mineralogy and origin of the magnetic fabric

The studied samples display three distinct behaviors, with the predominance of behavior number two, where temperature transitions suggest hematite and possibly Ti-magnetite as the main magnetic minerals present in our samples. In this group of samples, IRM curves indicate a considerable amount of high-coercivity phases (Fig. 6E) and display a typical behavior of hematite presence (e.g., Raposo and Egydio-Silva, 2001). Hysteresis loops suggest a mixture of high and low-coercivity components marked by a distinct wasp-waisted pattern (Fig. 6F; Roberts et al., 1995; Tauxe et al., 1996).

Based on EDS data, estimations of the Curie temperature (T_C) in the Ti-magnetite and the corresponding ulvöspinel content (x) were performed using the Clark's formula (Clark, 1997):

$$Fe_{3-x}Ti_xO_4\ T_C\ (°C) = 578–580x - 150x^2$$

These estimations yield an average T_C of 516 °C, in agreement with the observed behavior of high-temperature thermomagnetic experiments, where a gradual decrease in magnetic susceptibility occurs above these temperatures (Fig. 6D,G).

In one site, FORC data suggests the presence of multi-domain grains (MD, Fig. 7A, Roberts et al., 2000; Muxworthy and Roberts, 2007), however in several samples, only a weakly magnetic component, small FORC distribution signal was detected (Fig. 7B), which could be linked to the small amount of magnetic phases in the studied samples. This seems to be supported by the low bulk magnetic susceptibility values, which are usually $<100 \times 10^{-6}$ SI (Fig. 9A), and the small Fe contents in the chemical analyses (Table 1). Such low bulk magnetic susceptibility values are comparable to rocks where paramagnetic minerals (such as biotite, amphibole, pyroxene and olivine) dominate as the main magnetic susceptibility and, potentially, AMS carriers (e.g., Syono, 1960; Rochette et al., 1992; Aydin et al., 2007). However, petrographic observations reveal an absence of such paramagnetic phases in the studied samples, suggesting that the observed low bulk susceptibility values are in fact, linked to the small number of ferromagnetic minerals.

Based on the SEM, EDS and magnetic mineralogy analyses, our data points to hematite and Ti-magnetite crystals as the predominant carriers of the AMS signal, considering the observed amount, orientation and distribution of these magnetic phases.

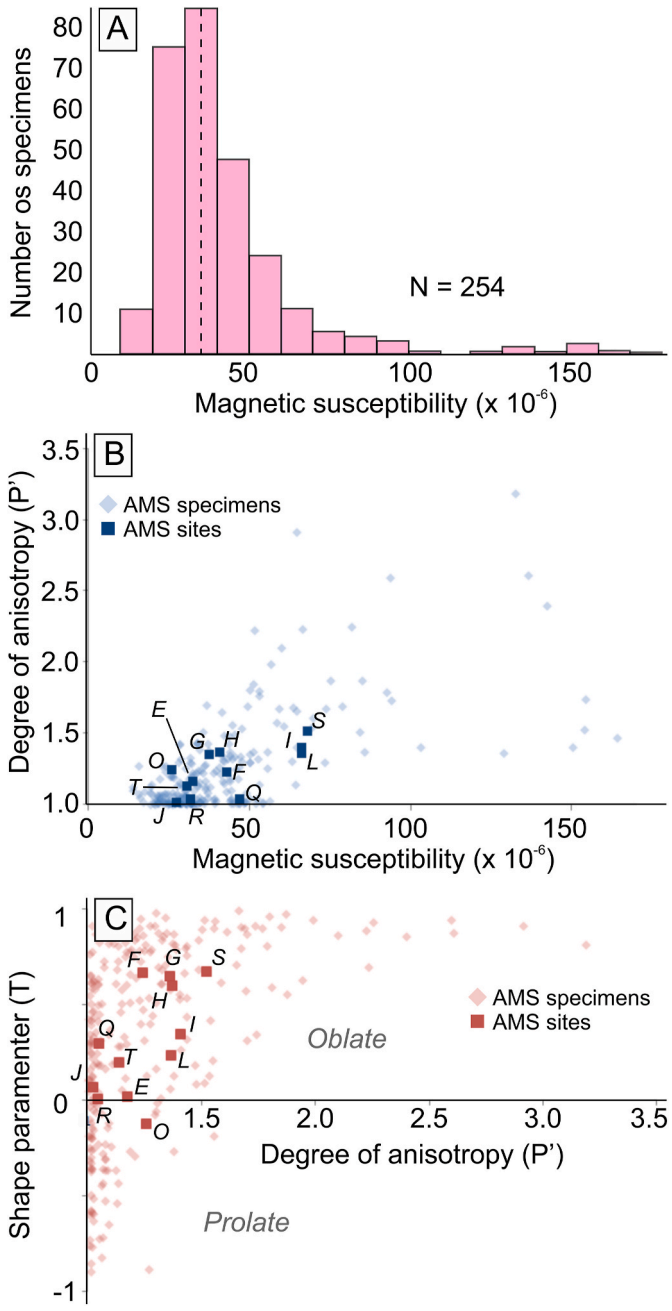

Fig. 9. Scalar results of AMS analyses: (A) histogram showing the distribution of the magnetic susceptibility in the measures samples; (B) degree of anisotropy and magnetic susceptibility plot; (C) shape parameter and degree of anisotropy plot.

5.5. AMS and structural data

Since no tectonic fabric was identified in the outcrop, we interpreted the AMS results as a record of the magmatic viscous strain during the flow emplacement (Dragoni et al., 1997; Paterson et al., 1998; Borradaile and Jackson, 2010; Cañón-Tapia, 2005). The low mean magnetic susceptibility and distribution of Km values (Fig. 9A) is common for rhyolites, and can be related to variable oxidation stages inside a given flow unit (Clark, 1997), also suggesting a small contribution of ferromagnetic minerals.

In order to assist the emplacement evaluation, Fig. 11 presents the field distribution of both structural (field) and magnetic fabric data on CP flow. Overall, the flow presents a predominance of sub-vertical foliation planes, a pattern consistent along the entire outcrop area, which is confirmed by both field (Fig. 11A) and AMS data (Fig. 11B). The observed folds also follow this structural pattern, as hinge lines tend to display NNW-SSE trending orientations (Fig. 11A). Despite this general sub-vertical pattern, several locations present variable field and AMS strike orientations of foliations, reflecting the structural complexity of CP flows (Figs. 10 and 11A,B).

The predominance of oblate ellipsoids ($T > 0$, Fig. 9C) matches the field observations, where linear features were almost absent. This predominance of oblate ellipsoids in crystal-poor rhyolites seems to be confirmed by other AMS studies performed in analogous flows (e.g., Cañón-Tapia and Castro, 2004; Shields et al., 2016). Analyzing the T parameter, Cañón-Tapia and Castro (2004) associate the progressive development of oblate fabrics with the dispersion o microlites along the shear planes of flow. In addition to the flow regime, the observed predominance of oblate ellipsoids suggests the presence of intrinsically oblate magnetic phase as the AMS carrier, such as hematite (Guerrero-Suarez and Martín-Hernández, 2012).

The average P′ is 1.25 (25%), a relatively high value when compared to other reported AMS results for silicic flows, which usually present maximum (at a specimen level) P′ values < 1.5 (e.g. Cañón-Tapia and Castro, 2004; Shields et al., 2016; Tomek et al., 2016; Cañón-Tapia and Raposo, 2018; Guimarães et al., 2018). Some of the observed high P′ values in CP are comparable to AMS measurement in shear zones (Mertanen and Karell, 2011), which suggests the occurrence of high-strain zones within the studied flow. The development of high P′ zones was also observed in the Rocche Rosse flow (in Lipari, Italy), where values of P' > 15% can be observed in the middle and upper section of the flow (Shields et al., 2016).

These zones could represent strain-softening regions (Fig. 11D) in the flow, which are ultimately linked to the non-Newtonian behavior of silicate melts (Castro and Cashman, 1999; Sonder et al., 2006). However, we also observe a considerable variation in P′ values (even when considering the same sampling core and site), suggesting that strain distribution in CP flow was highly heterogeneous, producing P′ differences down to an AMS specimen scale (~2.5 cm). As revealed by petrographic analysis, crystals occur along the foliation planes of flow, frequently forming trains (Fig. 3B and C). The presence of these layers could influence strain distribution, producing localized strain zones in the crystal-melt interface (Castro and Cashman, 1999). Please note that only oblate ellipsoids display high P′ values (P > 50%), indicating that flow-induced strain was preferably accommodated through flattening (Figs. 9C and 11C).

Contour plots were applied in order to define general trends in the flow (Fig. 12). Considering all measured specimens, there is a clear predominance of sub-vertical planes, with K_3 persistently showing an ESE sub-horizontal plunge (Fig. 12A). We used the shape parameter as a criterion to analyze each ellipsoid format separately. The magnetic lineation of prolate ellipsoids (K_1) reveals a NE-SW alignment (Fig. 12B), which could be associated with a radial stretching along the NE-SW axis (Buisson and Merle, 2004). Oblate ellipsoids are represented by NNE-SSW trending magnetic foliations, and high dip values, defined by the predominance of low plunge, ENE and ESE trending, K_3 axes (Fig. 12C).

To examine the orientation of high-strain ellipsoids (magnetic anisotropy degree > 50%), which account for 15% of all measured specimens, we also build a contour plot using only ellipsoids with P' > 1.5 (Fig. 12D). High-strain ellipsoids display similar orientation when compared to foliations obtained using all ellipsoids (Fig. 12A and C), suggesting the presence of high strain zones with a consistent NE-SW orientation within the CP flow. Such zones are observed in modern flows and can act as breakout zones for new lobes in a complex flow unit, usually related to the flow front (Tuffen et al., 2013; Leggett et al., 2020). Since both flow foliations and the axial planes of flow-induced folds are expected to form trending perpendicular to flow direction (Christiansen and Lipman, 1966; Smith and Houston, 1994; Smith,

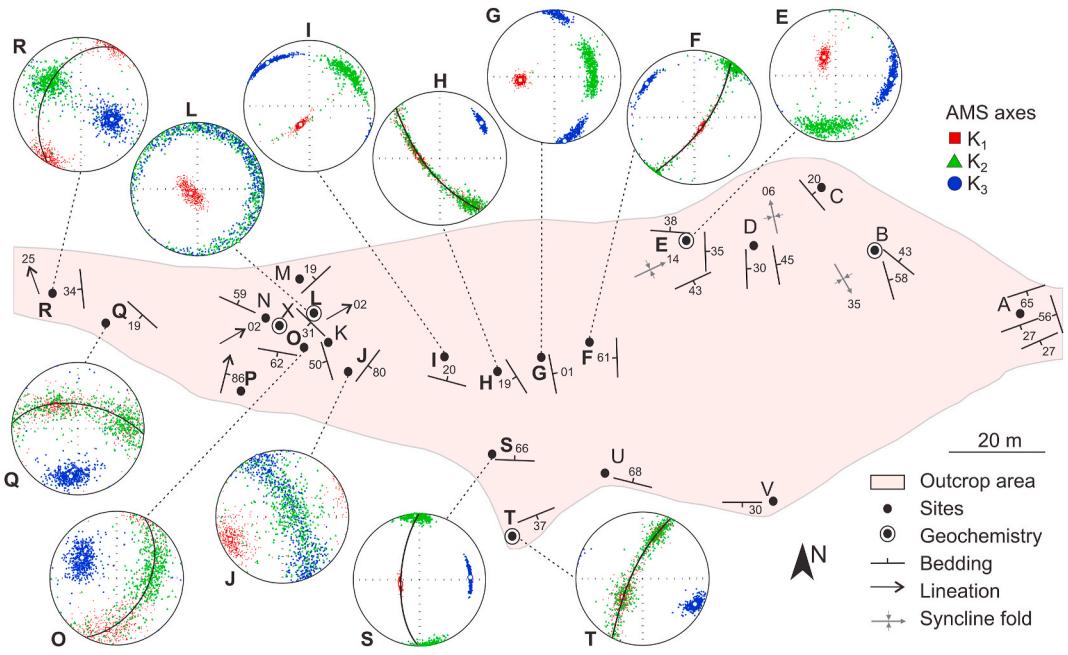

Fig. 10. Overview of the structural data collected at CP and lower hemispheres stereo plots of AMS results (geographical orientation). Black lines represent the projection of the magnetic foliation in the stereo plots. Site L presents two geochemistry samples.

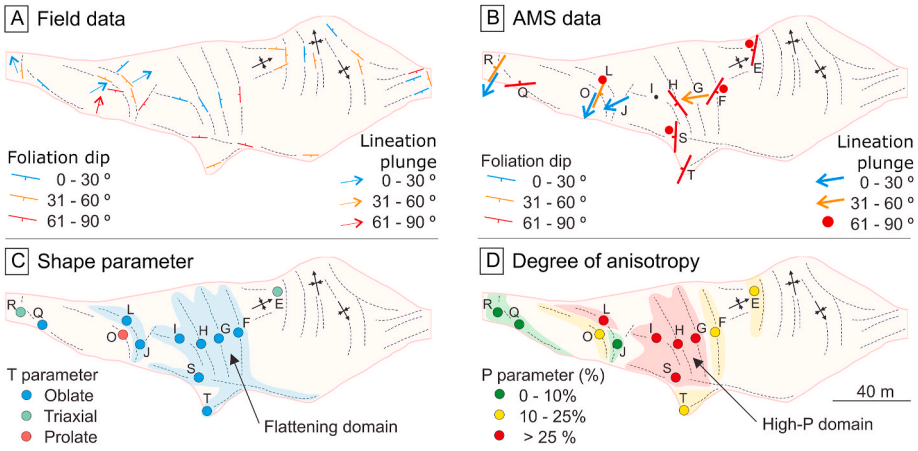

Fig. 11. Maps of the main structural data showing (A) compass data, (B) AMS data, (C) shape parameter and (D) degree of anisotropy distribution in CP flow.

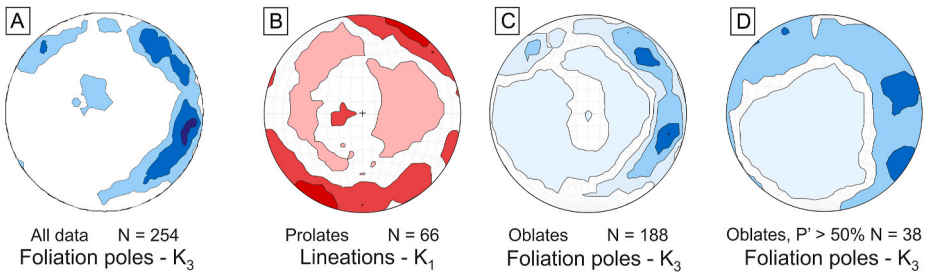

Fig. 12. Contour plots of AMS data, including (A) K_3 using all data, (B) K_1 using only prolate ellipsoids, (C) K_3 using only oblate ellipsoids and (D) K_3 using only oblate ellipsoids with P' > 50%.

1996; Fink, 1980), we can estimate a NW-SE flow direction for CP flows.

Despite the absence of brittle structures (which may suggest a marginal section of a given flow), both AMS results (marked by high P′ values) and field data (highlighted by the distinctive presence of folds) indicate a significant strain, which is expected to occur closer to the flow limits and substrate slope changes (Fink, 1980; Ventura et al., 1996; Leggett et al., 2020). These features may suggest an important role of the flow crust over the thermal evolution of CP flow, granting efficient thermal insulation and promoting slow cooling rates and viscous deformation even next to the flow limits, as reported by field

observations on modern flows (Tuffen et al., 2013; Magnall et al., 2018).

5.6. Integrated emplacement model

Fieldwork and rheology data indicates that most flow-induced deformation of CP flows were accommodated through viscous flows, above the T_g (approximately 750 °C), which is attested by the presence of continuous flow layers and the absence of brittle features, as observed in both field features and petrographic analyses. The low crystal content of CP suggests its emplacement as an obsidian flow, with little to none effect of crystals on the overall melt rheology (Castruccio et al., 2010). This observation also allows us to constrain CP emplacement as either a viscosity of a crust yield strength-controlled flow (*sensu* Magnall et al., 2017).

The presence of distinct folds with variable sizes and wavelengths suggests some degree of rheological contrast among the flow layers (Fink, 1980; Dragoni et al., 1992), with minimum emplacement viscosity estimations of 10^8 Pa s. The flow-induced deformation is predominantly recorded by the silicate fabric, resulting in an AMS signal that shows a preferentially NW-SE flow direction, with the distinct presence of high-dipping foliations. In addition, the vergence of folds, as well as field (Fig. 11A) and magnetic planes (Figs. 11B and 12A) allow us to constrain the sense of flow toward ESE (e.g., Fink, 1983). The scarce occurrence of both magnetic and field lineations, along with the predominance of oblate ellipsoids suggests an overall flattening regime, which includes the presence of high-strain zones marked by a high degree of anisotropy. This high anisotropy degree pattern was also observed by Cañón-Tapia and Castro (2004) and Shield et al. (2016), suggesting a more local accommodation of strain in obsidian flows. The overall presence of upright folds and general vergence of foliations in the outcrop indicates that the exposed CP area may represent the upper region of a rhyolite flow unit (Christiansen and Lipman, 1966; Fink, 1980, 1983) (Fig. 13).

6. Final remarks

Using the multiproxy approach involving fieldwork, structural, geochemistry, rheology and magnetic fabric analyses, we were able to constrain the emplacement of the ancient Neoproterozoic CP rhyolitic flow, despite its structural complexity. Our data suggest the CP emplacement as an obsidian flow, and the current exposure likely represents the near-vent area of this flow.

Especially in rhyolites, which usually present the development of complex magmatic structures, determining the degree and orientation of strain can be particularly difficult (Shields et al., 2016). These difficulties may be increased when dealing with ancient, partially preserved flows, as the case of much Neoproterozoic volcanism in Southern Brazil (Lima et al., 2007) and around the world. In this work, we apply a set of techniques that allow a comprehensive evaluation of rhyolite flows, which may be useful to the study of several ancient flows. The information that can be retrieved using this approach include rheological estimations (T_L and viscosity), the minimum emplacement temperatures (T_g), and the strain distribution, character and orientation in the flow (obtained using magnetic fabrics), all useful information that can help us improve our knowledge about the emplacement mechanisms or rhyolitic flows. As noted by Cañón-Tapia and Castro (2004), the AMS has been extensively applied to the study of basaltic flows, while felsic systems remain relatively unexplored by this technique. In this sense, this contribution also aims to add to our general knowledge about AMS fabrics and its behavior in felsic systems.

Our data shows that CP emplacement occurred with little to none flow movement after crossing T_g (Giordano et al., 2005), due to the overall absence of brittle structures. Structural patterns based on fieldwork and AMS data suggests that the observed section of CP flow may represent the upper region of an ancient rhyolitic flow (Christiansen and Lipman, 1966; Fink, 1980). The distinct presence of high-dipping foliations and the absence of lineations and predominance of AMS oblate ellipsoids suggests an overall flattening regime, including the occurrence of high-strain zones within the flow, which could be linked to viscosity-contrasting layers.

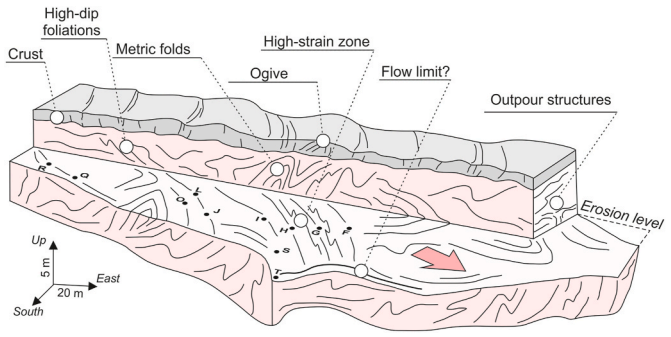

Fig. 13. Emplacement model for Cerro do Perau outcrop flow, with the AMS sites. Red arrow indicates the inferred flow direction. (For interpretation of the references to color in this figure legend, the reader is referred to the Web version of this article.)

Declaration of competing interest

The authors declare that they have no known competing financial interests or personal relationships that could have appeared to influence the work reported in this paper.

Acknowledgments

We would like to thank the reviewers Eric Ferré and Irine Raposo, and the editors Augusto Rapalini and Andres Folguera for their comments and careful review, which helped improve the manuscript. This work was partially funded by the Brazilian National Council for Scientific and Technological Development (CNPq), projects 303015/2015-2, 441766/2014-5, 304036/2018-8, and 406925/2018-6.

Appendix A. Supplementary data

Supplementary data to this article can be found online at https://doi.org/10.1016/j.jsames.2020.102982.

Author statement

Mauricio Haag: AMS analysis, Data processing, Writting and Fieldwork. Rayane Freitas: Geochemical analyses, Sample preparation, SEM analysis and Fieldwork. Carlos Sommer: Conceptualization, Geochemical interpretation, Reviewing and Editing, Fieldwork. Jairo Savian: Magnetic mineralogy interpretation, Reviewing and Editing, Fieldwork. Evandro Lima: Conceptualization, Reviewing and Editing, Fieldwork. Johnathan Gambeta: FORC analysis and interpretation. Diego Lyra: Structural analysis, Fieldwork. Ricardo da Trindade: Magnetic mineralogy interpretation and supervision.

References

Alva-Valdivia, L.M., Agarwal, A., Caballero-Miranda, C., García-Amador, B.I., Morales-Barrera, W., Rodríguez-Elizarraráz, S., Rodríguez-Trejo, A., 2017. Paleomagnetic and AMS studies of the El Castillo ignimbrite, central-east Mexico: source and rock magnetic nature. J. Volcanol. Geoth. Res. 336, 140–154. https://doi.org/10.1016/j.jvolgeores.2017.02.014.

Aydin, A., Ferré, E.C., Aslan, Z., 2007. The magnetic susceptibility of granitic rocks as a proxy for geochemical composition: example from the Saruhan granitoids, NE Turkey. Tectonophysics 441, 85–95. https://doi.org/10.1016/j.tecto.2007.04.009.

Bernardi, M.I., Bertotto, G.W., Jalowitzki, T.L.R., Orihashi, Y., Ponce, A.D., 2015. Emplacement history and inflation evidence of a long basaltic lava flow located in Southern Payenia Volcanic Province, Argentina. J. Volcanol. Geoth. Res. 293, 46–56. https://doi.org/10.1016/j.jvolgeores.2015.02.001.

Besser, M.L., Vasconcellos, E.M.G., Nardy, A.J.R., 2018. Morphology and stratigraphy of serra geral silicic lava flows in the northern segment of the torres trough, Paraná igneous province. Braz. J. Genet. 48, 201–219. https://doi.org/10.1590/2317-4889201820180087.

Borradaile, G.J., Jackson, M., 2010. Structural geology, petrofabrics and magnetic fabrics (AMS, AARM, AIRM). J. Struct. Geol. 32, 1519–1551. https://doi.org/10.1016/j.jsg.2009.09.006.

Bryan, S.E., Riley, T.R., Jerram, D.A., Leat, P.T., Stephens, C.J., 2002. Silicic volcanism: an undervalued component of Large Igneous Provinces and volcanic rifted margins. In: Menzies, M.A., Klemperer, S.L., Ebinger, C.J., Baker, J. (Eds.), Volcanic Rifted Margins. Geol. Soc. Am. Spec. Pap., vol. 362, pp. 99–120.

Buisson, C., Merle, O., 2004. Numerical simulation of strain within lava domes. J. Struct. Geol. 26, 847–853. https://doi.org/10.1016/j.jsg.2003.11.017.

Bullock, L.A., Gertisser, R., O'Driscoll, B., 2018. Emplacement of the Rocche Rosse rhyolite lava flow (Lipari, Aeolian Islands). Bull. Volcanol. 80 https://doi.org/10.1007/s00445-018-1222-4.

Cañón-Tapia, E., 2005. Uses of anisotropy of magnetic susceptibility in the study of emplacement processes of lava flows. In: Special Paper 396: Kinematics and Dynamics of Lava Flows. Geological Society of America, pp. 29–46. https://doi.org/10.1130/0-8137-2396-5.29.

Cañón-Tapia, E., Castro, J., 2004. AMS measurements on obsidian from the Inyo Domes, CA: a comparison of magnetic and mineral preferred orientation fabrics. J. Volcanol. Geoth. Res. 134, 169–182. https://doi.org/10.1016/j.jvolgeores.2004.01.005t. Mexico: Source and rock magnetic nature. Journal of Volcanology and Geothermal Research 336, 140–154. 10.1016/j.jvolgeores.2017.02.014.

Cañón-Tapia, E., Raposo, M.I.B., 2018. Anisotropy of magnetic susceptibility of silicic rocks from quarries in the vicinity of São Marcos, Rio Grande do Sul, South Brazil: implications for emplacement mechanisms. J. Volcanol. Geoth. Res. 355, 165–180. https://doi.org/10.1016/j.jvolgeores.2017.07.018.

Cardozo, N., Allmendinger, R.W., 2013. Spherical projections with OSXStereonet. Comput. Geosci. 51, 193–205. https://doi.org/10.1016/j.cageo.2012.07.021.

Cas, R.A.F., Wright, J.V., 1987. Volcanic Successions Modern and Ancient. Springer Netherlands. https://doi.org/10.1007/978-94-009-3167-1.

Cassidy, M., Manga, M., Cashman, K., Bachmann, O., 2018. Controls on explosive-effusive volcanic eruption styles. Nat. Commun. 9 https://doi.org/10.1038/s41467-018-05293-3.

Castro, J., Cashman, K.V., 1999. Constraints on rheology of obsidian lavas based on mesoscopic folds. J. Struct. Geol. 21, 807–819. https://doi.org/10.1016/s0191-8141(99)00070-x.

Castruccio, A., Rust, A.C., Sparks, R.S.J., 2010. Rheology and flow of crystal-bearing lavas: insights from analogue gravity currents. Earth Planet Sci. Lett. 297, 471–480. https://doi.org/10.1016/j.epsl.2010.06.051.

Christiansen, R.L., Lipman, P.W., 1966. Emplacement and thermal history of a rhyolite flow near Fortymile Canyon, southern Nevada. Geol. Soc. Am. Bull. 77, 671–684. https://doi.org/10.1130/0016-7606(1966)77[671:EATHOA]2.0.CO;2.

Clark, D.A., 1997. Magnetic petrophysics and magnetic petrology; aids to geological interpretation of magnetic surveys. AGSO J. Aust. Geol. Geophys. 17, 83–103.

De la Roche, H., Leterrier, J., Grandclaude, P., Marchal, M., 1980. A classification of volcanic and plutonic rocks using R 1 R 2 -diagram and major-element analyses — its relationships with current nomenclature. Chem. Geol. 29, 183–210. https://doi.org/10.1016/0009-2541(80)90020-0.

Di Genova, D., Kolzenburg, S., Wiesmaier, S., Dallanave, E., Neuville, D.R., Hess, K.U., Dingwell, D.B., 2017. A compositional tipping point governing the mobilization and eruption style of rhyolitic magma. Nature 552, 235–238. https://doi.org/10.1038/nature24488.

Dragoni, M., Lanza, R., Tallarico, A., 1997. Magnetic anisotropy produced by magma flow: theoretical model and experimental data from Ferrar dolerite sills (Antarctica). Geophys. J. Int. 128, 230–240. https://doi.org/10.1111/j.1365-246x.1997.tb04083.x.

Dragoni, M., Pondrelli, S., Tallarico, A., 1992. Longitudinal deformation of a lava flow: the influence of Bingham theology. J. Volcanol. Geoth. Res. 52, 247–254. https://doi.org/10.1016/0377-0273(92)90047-H.

Elston, W.E., Smith, E.I., 1970. Determination of flow direction of rhyolitic ash-flow tuffs from fluidal textures. Geol. Soc. Am. Bull. 81, 3393–3406.

Ewart, A., 1979. A review of the mineralogy and chemistry of tertiary-recent dacitic, latitic, rhyolitic, and related salic volcanic rocks. In: Developments in Petrology. Elsevier, pp. 13–121. https://doi.org/10.1016/b978-0-444-41765-7.50007-1.

Fink, J., 1980. Surface folding and viscosity of rhyolite flows. Geology 8, 250. https://doi.org/10.1130/0091-7613(1980)8<250:sfavor>2.0.co;2.

Fink, J.H., 1983. Structure and emplacement of a rhyolitic obsidian flow: little glass mountain, medicine lake highland, northern California. Geol. Soc. Am. Bull. 94, 362. https://doi.org/10.1130/0016-7606(1983)94<362:saeoar>2.0.co;2.

Fink, J.H., Manley, C.R., 1987. Origin of pumiceous and glassy textures in rhyolite flows and domes. In: Fink, J.H. (Ed.), Emplacement of Silicic Domes and Lava Flows, pp. 77–88. Spec. Pap. Geol. Soc. Am. 212.

Finn, D.R., Coe, R.S., Kelly, H., Branney, M., Knott, T., Reichow, M., 2015. Magnetic anisotropy in rhyolitic ignimbrite, Snake River Plain: implications for using remanent magnetism of volcanic rocks for correlation, paleomagnetic studies, and geological reconstructions. J. Geophys. Res.: Solid Earth 120, 4014–4033. https://doi.org/10.1002/2014jb011868.

Giordano, D., Mangiacapra, A., Potuzak, M., Russell, J.K., Romano, C., Dingwell, D.B., Di Muro, A., 2006. An expanded non-Arrhenian model for silicate melt viscosity: a treatment for metaluminous, peraluminous and peralkaline liquids. Chem. Geol. 229, 42–56. https://doi.org/10.1016/j.chemgeo.2006.01.007.

Giordano, D., Nichols, A.R.L., Dingwell, D.B., 2005. Glass transition temperatures of natural hydrous melts: a relationship with shear viscosity and implications for the welding process. J. Volcanol. Geoth. Res. 142, 105–118. https://doi.org/10.1016/j.jvolgeores.2004.10.015.

Giordano, D., Russell, J.K., Dingwell, D.B., 2008. Viscosity of magmatic liquids: a model. Earth Planet Sci. Lett. 271 (1–4), 123–134. https://doi.org/10.1016/j.epsl.2008.03.038.

Gonnermann, H.M., Manga, M., 2007. The fluid mechanics inside a volcano. Annu. Rev. Fluid Mech. 39, 321–356. https://doi.org/10.1146/annurev.fluid.39.050905.110207.

Graham, J.W., 1954. Magnetic anisotropy, an unexploited petrofabric element. Geol. Soc. Am. Bull. 65, 1257–1258.

Guerrero-Suarez, S., Martín-Hernández, F., 2012. Magnetic anisotropy of hematite natural crystals: increasing low-field strength experiments. Int. J. Earth Sci. 101, 625–636. https://doi.org/10.1007/s00531-011-0666-y.

Guest, J.E., Duncan, A.M., Stofan, E.R., Anderson, S.W., 2012. Effect of slope on development of pahoehoe flow fields: evidence from Mount Etna. J. Volcanol. Geoth. Res. 219 (220), 52–62. https://doi.org/10.1016/j.jvolgeores.2012.01.006.

Guimarães, L.F., Raposo, M.I.B., Janasi, V.A., Cañón-Tapia, E., Polo, L.A., 2018. An AMS study of different silicic units from the southern Paraná-Etendeka Magmatic Province in Brazil: implications for the identification of flow directions and local sources. J. Volcanol. Geoth. Res. 355, 304–318. https://doi.org/10.1016/j.jvolgeores.2017.11.014.

Harrison, R.J., Feinberg, J.M., 2008. FORCinel: an improved algorithm for calculating first-order reversal curve distributions using locally weighted regression smoothing. G-cubed 9. https://doi.org/10.1029/2008gc001987.

Hartmann, L.A., Chemale Jr., F., Philipp, R.P., 2007. Evolução geotectônica do Rio Grande do sul no Pré-cambriano. In: Ianuzzi, R., Frantz, J.C. (Eds.), 50 anos de Geologia, vol. 1. Editora Comunicação e Identidade, Porto Alegre, pp. 97–123.

Hrouda, F., Jelínek, V., Zapletal, K., 1997. Refined technique for susceptibility resolution into ferromagnetic and paramagnetic components based on susceptibility temperature-variation measurement. Geophys. J. Int. 129 (3), 715–719. https://doi.org/10.1111/j.1365-246X.1997.tb04506.x.

Hunt, C.P., Moskowitz, B.M., Banerjee, S.K., 1995. Magnetic properties of rocks and minerals. In: AGU Reference Shelf. American Geophysical Union, pp. 189–204. https://doi.org/10.1029/rf003p0189.

Janikian, L., de Almeida, R.P., da Trindade, R.I.F., Fragoso-Cesar, A.R.S., D'Agrella-Filho, M.S., Dantas, E.L., Tohver, E., 2008. The continental record of Ediacaran volcano-sedimentary successions in southern Brazil and their global implications. Terra. Nova 20, 259–266. https://doi.org/10.1111/j.1365-3121.2008.00814.x.

Jelinek, V., 1981. Characterization of the magnetic fabric of rocks. Tectonophysics 79, T63–T67. https://doi.org/10.1016/0040-1951(81)90110-4.

Lattard, D., Engelmann, R., Kontny, A., Sauerzapf, U., 2006. Curie temperatures of synthetic titanomagnetites in the Fe-Ti-O system: effects of composition, crystal chemistry, and thermomagnetic methods. J. Geophys. Res. 111 https://doi.org/10.1029/2006jb004591 n/a-n/a.

Lejeune, A.-M., Richet, P., 1995. Rheology of crystal-bearing silicate melts: an experimental study at high viscosities. J. Geophys. Res.: Solid Earth 100, 4215–4229.

Leggett, T.N., Befus, K.S., Kenderes, S.M., 2020. Rhyolite lava emplacement dynamics inferred from surface morphology. J. Volcanol. Geoth. Res. https://doi.org/10.1016/j.jvolgeores.2020.106850, 106850.

Lima, E.F., Sommer, C.A., Nardi, L.V.S., 2007. O vulcanismo neoproterozóico-ordoviciano no Escudo Sul-riograndense: os ciclos vulcânicos da Bacia do Camaquã. In: Iannuzzi, R., Frantz, J.C. (Eds.), 50 Anos de Geologia. Instituto de Geociências. Contribuições. Porto Alegre, Comunicação e Identidade, pp. 79–95.

Magnall, N., James, M.R., Tuffen, H., Vye-Brown, C., 2017. Emplacing a cooling-limited rhyolite lava flow: similarities with basaltic lava flows. Front. Earth Sci. 5 https://doi.org/10.3389/feart.2017.00044.

Magnall, N., James, M.R., Tuffen, H., Vye-Brown, C., Schipper, C.I., Castro, J.M., Davies, A.G., 2018. The origin and evolution of breakouts in a cooling-limited rhyolite lava flow. GSA Bulletin 131, 137–154. https://doi.org/10.1130/b31931.1.

Mahood, G., Hildreth, W., 1983. Large partition coefficients for trace elements in high-silica rhyolites. Geochem. Cosmochim. Acta 47, 11–30. https://doi.org/10.1016/0016-7037(83)90087-x.

Manley, C.R., 1992. Extended cooling and viscous flow of large, hot rhyolite lavas: implications of numerical modeling results. J. Volcanol. Geoth. Res. 53, 27–46. https://doi.org/10.1016/0377-0273(92)90072-l.

Manley, C.R., Fink, J.H., 1987. Internal textures of rhyolite flows as revealed by research drilling. Geology 15, 549. https://doi.org/10.1130/0091-7613(1987)15<549:itorfa>2.0.co;2.

Matté, V., Sommer, C.A., Lima, E.F. de, Philipp, R.P., Basei, M.A.S., 2016. Post-collisional ediacaran volcanism in oriental Ramada Plateau, southern Brazil. J. S. Am. Earth Sci. 71, 201–222. https://doi.org/10.1016/j.jsames.2016.07.015.

Mertanen, S., Karell, F., 2011. Rock magnetic investigations constraining relative timing for gold deposits in Finland. Bull. Geol. Soc. Finland 83, 75–94.

Moncinhatto, T.R., Haag, M.B., Hartmann, G.A., Savian, J.F., Poletti, W., Sommer, C.A., Caselli, A.T., Trindade, R.I.F., 2020. Mineralogical control on the magnetic anisotropy of lavas and ignimbrites: a case study in the Caviahue-Copahue field (Argentina). Geophys. J. Int. 220, 821–838. https://doi.org/10.1093/gji/ggz483.

Muxworthy, A.R., Roberts, A.P., 2007. First-order reversal curve (FORC) diagrams. In: Gubbins, D., Herrero-Bervera, E. (Eds.), Encyclopedia of Geomagnetism and Paleomagnetism. Springer, Dordrecht, Netherlands, pp. 266–272.

Nakagawa, M., Amma-miyasaka, M., Tomijima, C., Matsumoto, A., Hase, R., 2018. Eruption sequence of the 46 ka caldera-forming eruption of Shikotsu volcano, inferred from stratigraphy of proximal deposits at South of lake Shikotsu, Japan. J. Geogr. 127, 247–271. https://doi.org/10.5026/jgeography.127.247.

Paterson, S.R., Fowler Jr., T.K., Schmidt, K.L., Yoshinobu, A.S., Yuan, E.S., Miller, R.B., 1998. Interpreting magmatic fabric patterns in plutons. Lithos 44, 53–82. https://doi.org/10.1016/s0024-4937(98)00022-x.

Patiño Douce, A.E., 1997. Generation of metaluminous A-type granites by low-pressure melting of calc-alkaline granitoids. Geology 25, 743. https://doi.org/10.1130/0091-7613(1997)025<0743:gomatg>2.3.co;2.
Pearce, J.A., Harris, N.B.W., Tindle, A.G., 1984. Trace element discrimination diagrams for the tectonic interpretation of granitic rocks. J. Petrol. 25, 956–983. https://doi.org/10.1093/petrology/25.4.956.
Petrovsky, E., Kapicka, A., 2006. On determination of the Curie point from thermomagnetic curves. J. Geophys. Res. 111, B12S27. https://doi.org/10.1029/2006JB004507.
Pinkerton, H., Sparks, R.S.J., 1978. Field measurements of the rheology of lava. Nature 276, 383–385. https://doi.org/10.1038/276383a0.
Raposo, M.I.B., Egydio-Silva, M., 2001. Magnetic fabric studies of high-grade metamorphic rocks from the Juiz de Fora complex, Ribeira belt, Southeastern Brazil. Int. Geol. Rev. 43, 441–456. https://doi.org/10.1080/00206810109465025.
Roberts, A.P., Cui, Y., Verosub, K.L., 1995. Wasp-waisted hysteresis loops: mineral magnetic characteristics and discrimination of components in mixed magnetic systems. J. Geophys. Res.: Solid Earth 100, 17909–17924. https://doi.org/10.1029/95jb00672.
Roberts, A.P., Pike, C.R., Verosub, K.L., 2000. First-order reversal curve diagrams: a new tool for characterizing the magnetic properties of natural samples. J. Geophys. Res.: Solid Earth 105, 28461–28475. https://doi.org/10.1029/2000jb900326.
Roberts, A.P., Almeida, T.P., Church, N.S., Harrison, R.J., Heslop, D., Li, Y., Li, J., Muxworthy, A.R., Williams, W., Zhao, X., 2017. Resolving the origin of pseudo-single domain magnetic behavior. J. Geophys. Res.: Solid Earth 122, 9534–9558. https://doi.org/10.1002/2017JB014860.
Roberts, A.P., Tauxe, L., Heslop, D., Zhao, X., Jiang, Z., 2018. A critical appraisal of the "Day" diagram. J. Geophys. Res.: Solid Earth 123, 2618–2644. https://doi.org/10.1002/2017JB015247.
Roberts, A.P., Hu, P., Harrison, R.J., Heslop, D., Muxworthy, A.R., Oda, H., Sato, T., Tauxe, L., Zhao, X., 2019. Domain state diagnosis in rock magnetism: evaluation ofpotential alternatives to the Day diagram. J. Geophys. Res.: Solid Earth 124, 5286–5314. https://doi.org/10.1029/2018JB017049.
Rochette, P., Jackson, M., Aubourg, C., 1992. Rock magnetism and the interpretation of anisotropy of magnetic susceptibility. Rev. Geophys. 30, 209. https://doi.org/10.1029/92rg00733.
Rochette, P., Aubourg, C., Perrin, M., 1999. Is this magnetic fabric normal? A review andcase studies in volcanic formations. Tectonophysics 307, 219–234. https://doi.org/10.1016/S0040-1951(99)00127-4.
Shields, J.K., Mader, H.M., Caricchi, L., Tuffen, H., Mueller, S., Pistone, M., Baumgartner, L., 2016. Unravelling textural heterogeneity in obsidian: shear-induced outgassing in the Rocche Rosse flow. J. Volcanol. Geoth. Res. 310, 137–158. https://doi.org/10.1016/j.jvolgeores.2015.12.003.
Single, R.T., Jerram, D.A., 2004. The 3D facies architecture of flood basalt provinces and their internal heterogeneity: examples from the Palaeogene Skye Lava Field. J. Geol. Soc. 161, 911–926. https://doi.org/10.1144/0016-764903-136.
Sisson, T.W., Grove, T.L., 1993. Temperatures and H2O contents of low-MgO high-alumina basalts. Contrib. Mineral. Petrol. 113 (2), 167–184. https://doi.org/10.1007/bf00283226.
Smith, J.V., 1996. Ductile-brittle transition structures in the basal shear zone of a rhyolite lava flow, eastern Australia. J. Volcanol. Geoth. Res. 72, 217–223. https://doi.org/10.1016/0377-0273(96)00009-1.
Smith, J.V., Houston, E.C., 1994. Folds produced by gravity spreading of a banded rhyolite lava flow. J. Volcanol. Geoth. Res. 63, 89–94. https://doi.org/10.1016/0377-0273(94)90019-1.
Sommer, C.A., Lima, E.F., Nardi, L.V.S., 1999. Evolução do vulcanismo alcalino na porção sul do Platô do Taquarembó, Dom Pedrito - RS. Rev. Bras. Geociencias 29 (2), 245–254.
Sommer, C.A., Lima, E.F., Machado, A., Rossetti, L. de M.M., Pierosan, R., 2013. Recognition and characterization of high-grade ignimbrites from the Neoproterozoic rhyolitic volcanism in southernmost Brazil. J. S. Am. Earth Sci. 47, 152–165. https://doi.org/10.1016/j.jsames.2013.07.010.
Sommer, C.A., De Lima, E.F., Nardi, L.V.S., De Liz, J.D., Waichel, B.L., 2005. Neoproterozoic, mildly alkaline, bimodal volcanism in southern Brazil: geological and geochemical aspects. Int. Geol. Rev. 47, 1090–1110. https://doi.org/10.2747/0020-6814.47.10.1090.
Sommer, C.A., Nardi, L.V.S., Lima, E.F., 1993. O vulcanismo ácido alcalino do Platô do Taquarembó, Dom Pedrito, RS (ext. Abstr.). In: I Simp. Int. del Neoproterozóico–Cámbrico en la Cuenca del Plata. Rocha, pp. 40–45.
Sonder, I., Zimanowski, B., Büttner, R., 2006. Non-Newtonian viscosity of basaltic magma. Geophys. Res. Lett. 33 https://doi.org/10.1029/2005gl024240.
Syono, Y., 1960. Magnetic susceptibility of some rock forming silicate minerals such as amphiboles, biotites, cordierites and garnets. J. geomagn. geoelec 11, 85–93. https://doi.org/10.5636/jgg.11.85.
Tarling, D., Hrouda, F., 1993. Magnetic Anisotropy of Rocks. Springer.
Tauxe, L., Mullender, T.A.T., Pick, T., 1996. Potbellies, wasp-waists, and superparamagnetism in magnetic hysteresis. J. Geophys. Res. 101, 571–583.
Tauxe, L., Kylstra, N., Constable, C., 1991. Bootstrap statistics for paleomagnetic data. J. Geophys. Res. 96, 11723. https://doi.org/10.1029/91jb00572.
Tomek, F., Žák, J., Holub, F.V., Chlupáčová, M., Verner, K., 2016. Growth of intra-caldera lava domes controlled by various modes of caldera collapse, the Štiavnica volcano–plutonic complex, Western Carpathians. J. Volcanol. Geoth. Res. 311, 183–197. https://doi.org/10.1016/j.jvolgeores.2016.01.006.
Tuffen, H., James, M.R., Castro, J.M., Schipper, C.I., 2013. Exceptional mobility of an advancing rhyolitic obsidian flow at Cordón Caulle volcano in Chile. Nat. Commun. 4 https://doi.org/10.1038/ncomms3709.
Ventura, G., De Rosa, R., Colletta, E., Mazzuoli, R., 1996. Deformation patterns in a high-viscosity lava flow inferred from the crystal preferred orientation and imbrication structures: an example from Salina (the Aeolian Islands, southern Tyrrhenian Sea, Italy). Bull. Volcanol. 57, 555–562. https://doi.org/10.1007/bf00304439.
Vye-Brown, C., Self, S., Barry, T.L., 2013. Architecture and emplacement of flood basalt flow fields: case studies from the Columbia River Basalt Group, NW USA. Bull. Volcanol. 75 https://doi.org/10.1007/s00445-013-0697-2.
Walker, G.P.L., 1967. Thickness and viscosity of etnean lavas. Nature 213, 484–485. https://doi.org/10.1038/213484a0.
Whalen, J.B., Currie, K.L., Chappell, B.W., 1987. A-type granites: geochemical characteristics, discrimination and petrogenesis. Contrib. Mineral. Petrol. 95, 407–419. https://doi.org/10.1007/bf00402202.
Wildner, W., Lima, E., Nardi, L.V., Sommer, C.A., 2002. Volcanic cycles and setting in the Neoproterozoic III to Ordovician Camaquã Basin succession in southern Brazil: characteristics of post-collisional magmatism. J. Volcanol. Geoth. Res. 118, 261–283. https://doi.org/10.1016/s0377-0273(02)00259-7.
Wilson, C.J.N., Blake, S., Charlier, B.L.A., Sutton, A.N., 2005. The 26,5 ka Oruanui eruption, Taupo volcano, New Zealand: development, characteristics, and evacuation of a large rhyolitic magma body. J. Petrol. 47, 35–69. https://doi.org/10.1093/petrology/egi066.
Winchester, J.A., Floyd, P.A., 1977. Geochemical discrimination of different magma series and their differentiation products using immobile elements. Chem. Geol. 20, 325–343. https://doi.org/10.1016/0009-2541(77)90057-2.
Yang, R., Jiang, D., Lu, L.X., 2019. Constrictional strain and linear fabrics as a result of deformation partitioning: a multiscale modeling investigation and tectonic significance. Tectonics. https://doi.org/10.1029/2019tc005490.
Závada, P., Kratinová, Z., Kusbach, V., Schulmann, K., 2009. Internal fabric development in complex lava domes. Tectonophysics 466, 101–113. https://doi.org/10.1016/j.tecto.2008.07.005.
Zerfass, H., Almeida, D., del, PM. de., Gomes, C.H., 2000. Faciology of Acampamento Velho formation volcanic rocks (Camaquã Basin) in the region of Serra de Santa Barbara, Cerro do Perau and Cerro do Bugio (municipality of Caçapava do sul- RS). Rev. Bras. Geociencias 30, 12–16.